JGR Planets

RESEARCH ARTICLE
10.1029/2020JE006662

Seismic Efficiency for Simple Crater Formation in the Martian Top Crust Analog

A. Rajšić[1], K. Miljković[1], G. S. Collins[2], K. Wünnemann[3,4], I. J. Daubar[5], N. Wójcicka[2], and M. A. Wieczorek[6]

[1]School of Earth and Planetary Sciences, Space Science and Technology Center, Curtin University, Perth, Australia, [2]Department of Earth Science and Engineering, Imperial College London, London, UK, [3]Leibniz Institute for Evolution and Biodiversity Science, Museum für Naturkunde, Berlin, Germany, [4]Freie Universität Berlin, Institut für Geologische Wissenschaften, Germany, [5]Department of Earth, Environmental and Planetary Sciences, Brown University, Providence, RI, USA, [6]Observatoire de la Côte d'Azur, CNRS, Laboratoire Lagrange, Université Côte d'Azur, Nice, France

Key Points:

- Seismic efficiency decreases with the increase of porosity
- Seismic efficiency is ~8×10^{-4} in bedrock and ~4×10^{-7} to ~4×10^{-6} in highly porous regolith, for Martian simulants
- Pressure propagation is significantly dependent on the target's crushing strength, elastic threshold and speed sound, and resolution

Correspondence to:
A. Rajšić,
andrea.rajsic@postgrad.curtin.edu.au

Citation:
Rajšić, A., Miljković, K., Collins, G. S., Wünnemann, K., Daubar, I. J., Wójcicka, N., & Wieczorek, M. A. (2021). Seismic efficiency for simple crater formation in the Martian top crust analog. *Journal of Geophysical Research: Planets*, *126*, e2020JE006662. https://doi.org/10.1029/2020JE006662

Received 21 AUG 2020
Accepted 19 JAN 2021

Author Contributions:
Conceptualization: M. A. Wieczorek
Resources: I. J. Daubar
Supervision: K. Miljković, G. S. Collins, K. Wünnemann
Validation: N. Wójcicka

Abstract The first seismometer operating on the surface of another planet was deployed by the NASA InSight (Interior Exploration using Seismic Investigations, Geodesy and Heat Transport) mission to Mars. It gives us an opportunity to investigate the seismicity of Mars, including any seismic activity caused by small meteorite bombardment. Detectability of impact generated seismic signals is closely related to the seismic efficiency, defined as the fraction of the impactor's kinetic energy transferred into the seismic energy in a target medium. This work investigated the seismic efficiency of the Martian near surface associated with small meteorite impacts on Mars. We used the iSALE-2D (Impact-Simplified Arbitrary Lagrangian Eulerian) shock physics code to simulate the formation of the meter-size impact craters, and we used a recently formed 1.5 m diameter crater as a case study. The Martian crust was simulated as unfractured nonporous bedrock, fractured bedrock with 25% porosity, and highly porous regolith with 44% and 65% porosity. We used appropriate strength and porosity models defined in previous works, and we identified that the seismic efficiency is very sensitive to the speed of sound and elastic threshold in the target medium. We constrained the value of the impact-related seismic efficiency to be between the order of ~10^{-7} to 10^{-6} for the regolith and ~10^{-4} to 10^{-3} for the bedrock. For new impacts occurring on Mars, this work can help understand the near-surface properties of the Martian crust, and it contributes to the understanding of impact detectability via seismic signals as a function of the target media.

Plain Language Summary Impact cratering is a common geological process on solid planetary bodies. When impact occurs, it releases shock waves into the target medium. The impactor's kinetic energy is spent on internal energy change (heating), plastic (irreversible) and elastic (reversible) deformation in the target. Seismic efficiency describes how much of the impact's kinetic energy is transferred into seismic energy. Having estimates for the values of the seismic efficiency in such events can help in further describing the properties of the Martian surface, particularly if impact conditions are known. In this work, we are using the iSALE-2D (Impact-Simplified Arbitrary Lagrangian Eulerian) shock physics code to simulate meter-size crater formation on Mars. Our results show that the pressure wave behaves differently in different target properties. The numerical simulation results showed that the seismic efficiency spans 2 orders of magnitude, for the investigated crater size range and target analog for the Martian bedrock and regolith.

1. Introduction

Since the successful landing of the NASA InSight (Interior Exploration using Seismic Investigations, Geodesy and Heat Transport) mission to Mars and the deployment of the Seismic Experiment for Interior Structure (SEIS) instrument (Banerdt et al., 2020; Lognonné et al., 2020), there is an opportunity to investigate the Martian interior in greater detail using seismology. There are several possible causes of seismicity on Mars, including thermal and lithostatic stresses caused by daily changes in temperature on this planet, recent volcanic activity (Knapmeyer-Endrun et al., 2017), and meteoroid impacts (I. Daubar et al., 2018; I. J. Daubar et al., 2013, 2014;, 2020; Malin et al., 2006).

On Mars, it is expected that only small, meter-to-decameter size, craters will form during lifetime of the InSight mission, considering the impact statistics and a given distance from the lander (I. J. Daubar et al., 2020; Stevanović et al., 2017; Teanby, 2015; Teanby & Wookey, 2011). The number of impact events detected by the InSight's seismometer was originally expected to be about a dozen (I. Daubar et al., 2018; Teanby, 2015; Teanby & Wookey, 2011). However, in response to the lack of detected impacts in the first year of InSight's operations, the number of expected impacts has been revised to approximately three detectable impact events per Earth year, with a large uncertainty on that estimate (I. J. Daubar et al., 2020). A possible reason for the lack of impact detections compared with prelanding estimates is that small impacts on Mars do not generate seismic signals as efficiently as previously assumed (Wójcicka et al., 2020).

A recently discovered 1.5 m crater on Mars, less than 40 km from the InSight lander, which formed during the period InSight was recording seismic data, has provided a test of InSight's impact-seismic detection threshold (I. J. Daubar et al., 2020). Although three candidate seismic events were identified in the time-window of the impact, none of them were definitively identified as impact related. Empirical and theoretical estimates of seismic moment and energy, together with preliminary wave propagation modeling, further concluded that detection of such a small impact 40 km from the lander was not expected given the range of seismic noise levels on Mars. However, how close to being detectable this impact event was not well understood.

One way to estimate the detectability of an impact generated seismic signal is from the seismic efficiency, k, which quantifies the fraction of the impact energy that is partitioned into seismic energy (e.g., McGarr et al., 1969; Schultz & Gault, 1975). Estimates of seismic efficiency of impacts from a variety of studies vary widely from 10^{-6} to 10^{-1} (I. Daubar et al., 2018; Güldemeister & Wünnemann, 2017; Hoerth et al., 2014; Matsue et al., 2020; McGarr et al., 1969; Pomeroy, 1963; Richardson & Kedar, 2013; Schultz & Gault, 1975; Shishkin, 2007; Yasui et al., 2015). High seismic efficiencies ($k > 10^{-3}$) are typically measured in explosions and nuclear tests in bedrock or highly consolidated materials (e.g., Patton & Walter, 1993), while low-seismic efficiencies ($k < 10^{-3}$) are seen in porous sediments or unconsolidated sands or soils (Latham et al., 1970; McGarr et al., 1969). While previous studies have shown that the seismic efficiency in the impact cratering process is dependent on the target properties (Güldemeister & Wünnemann, 2017; Miljković et al., 2019; Wójcicka et al., 2020), a systematic study of seismic efficiency for targets likely to be encountered on Mars is lacking. As a result, prelanding estimates of impact detections adopted "best-guess" seismic efficiencies for Mars of 2×10^{-5} (Teanby & Wookey, 2011) to 5×10^{-4} (I. Daubar et al., 2018; Teanby, 2015).

Seismic efficiency is intimately related to initial shock wave propagation (e.g., Pierazzo, 1997; Zel'dovich & Raizer, 2012). Holsapple (1993) defines the strong shock regimes when particle velocity in the target is larger than the speed of sound in the target. The pressure behavior is complex in the shock regime and its decays depend on both target and impact conditions (e.g., Holsapple, 1993; Holsapple & Housen, 2007; Prieur et al., 2017; Schmidt & Housen, 1987; Wünnemann et al., 2011). Beyond the shock regimes, starting several crater radii away, pressure continues to decay until the pressure is comparable to the local overburden pressure or material strength. This is the regime where the seismic efficiency can be estimated.

In this study, we numerically simulate small impacts on Mars to investigate the effect of target properties on stress wave decay and seismic efficiency. We use a similar modeling approach to Güldemeister and Wünnemann (2017) and Wójcicka et al. (2020) to determine seismic efficiency, which was previously shown to agree with laboratory experiments in porous rocks (Güldemeister & Wünnemann, 2017). We use the recently formed ~1.5-m crater on Mars (I. J. Daubar et al., 2020) as a case study to explore the seismic detectability of impacts from a range of different plausible surface materials. We also explore the sensitivity of stress wave decay to numerical resolution and material parameters.

2. Materials and Methods

In this study, we used the shock physics code iSALE-2D (Impact-Simplified Arbitrary Lagrangian Eulerian; https://isale-code.github.io/). The iSALE-2D code (Collins et al., 2004, 2005; Wünnemann et al., 2006) is a multirheology, multimaterial extension to the finite-difference hydrocode (Amsden et al., 1980). The iSALE shock physics code is validated against laboratory experiments (Güldemeister & Wünnemann, 2017; Wójcicka et al., 2020) at low- and high-strain rates, as well as other impact simulation codes (Pierazzo

Table 1
The Strength Model Parameters Used in Simulations for Different Targets, ROCK for the Bedrock (Collins et al., 2004) and LUNDD for the Regolith (Lundborg, 1968)

	Target			
Parameter	Nonporous bedrock	Fractured bedrock (25% porosity)	Highly porous regolith (44% porosity)	Highly porous regolith (65% porosity)
Strength model	ROCK	ROCK	LUNDD	LUNDD
Shear strength (damaged) (kPa)	10	0	10	0.3
Friction (damaged)	0.6	0.67	0.7	0.7
Limiting strength (damaged) (GPa)	3.5	0.17	0.25	0.25
Strength (intact) (MPa)	10	0.2	–	–
Friction (intact)	1.2	1.8	–	–
Limiting strength (intact) (GPa)	3.5	0.17	–	–
Crushing strength (kPa)	–	2×10^3	100	3

et al., 2008) and has been widely used to numerically simulate terrestrial impact crater formation (e.g., Collins et al., 2005; Cox et al., 2019; Wünnemann et al., 2006).

The computational domain is discretized by a grid of cells. The number of computational cells per projectile radius (CPPR) is commonly used to define the resolution of an impact simulation. The computational time depends on the size and resolution of the numerical mesh. We used two computational setups: (a) 3,000 × 3,000 cells in the high-resolution zone and 10 CPPR when modeling pressure wave propagation to several crater radii distance and (b) 600 × 600 cells and 12 CPPR when modeling crater formation. The crater formation can be simulated using CPPR between 10 and 20 without a significant influence on crater size and shape (Wünnemann et al., 2008). The simulations ran until after the transient crater formed and the pressure wave was several radii away from the impact point. Final crater sizes were estimated from known scaling laws (e.g., Holsapple, 1993; Prieur et al., 2017).

The impact speed at the upper atmosphere of Mars has an expected probability distribution with two peaks at about 5 and 11 km/s (I. Daubar et al., 2018;). During the lifetime of the InSight mission, it was expected that the largest crater diameter to form would likely be smaller than 30 m (I. Daubar et al., 2018; I. J. Daubar et al., 2013, 2014). For rocky meteoroids that form craters smaller than this size, atmospheric drag and ablation are expected to substantially reduce the impact speed on the ground to approximately 2–5 km/s (I. J. Daubar et al., 2020; Wójcicka et al., 2020). In this work, we used the ~1.5 m crater that formed on Mars in 2019 (I. J. Daubar et al., 2020) as a case study. For this particular crater on Mars, we adopt the impact conditions proposed by Wójcicka et al. (2020) of ~2 km/s impact speed at the ground level and a 4.4 cm radii projectile equivalent to 1 kg mass. To define these candidate values, they assumed a typical meteoroid density of 2.7 g/cm^3, preentry speed of 10 km/s, and angle of 45° to the horizontal and calculated the drag and ablation effects of the Martian atmosphere on the meteoroid, assuming that it did not fragment, using the methodology described by McMullan and Collins (2019). While we acknowledge that faster and slower impact speeds are possible, for example, if the meteoroid was much denser or underwent fragmentation, the value of 2 km/s we adopt here represents a typical ground impact speed for small rocky meteoroids to serve as a point of reference.

Furthermore, the impact condition to form a 1.5-m diameter crater on Mars could be estimated from known crater scaling relationships (e.g., Holsapple, 1993; Prieur et al., 2017; Teanby & Wookey, 2011). According to the standard scaling laws (Holsapple & Housen, 2007), the strength scaling for highly porous target where $\mu = 0.40$, $\upsilon = 0.4$, $Y = 1$ kPa, we used: $R / a = 0.725\left(Y / \rho U^2\right)^{-0.20}\left(\delta / \rho\right)^{0.40}$. For the 44% porous target, the impact condition used in this work can form a 1.5-m diameter crater. We maintained the same impact conditions for all target porosities. To describe projectile, we used the same strength model as the target (Lundborg strength model and Tillotson equation of state for basalt), but we did not include porosity in it (Table 1).

Surface investigations of the InSight landing area prior to the InSight landing approximated the thickness of the regolith to be 3–17 m (Golombek et al., 2017; Tanaka et al., 2014; Warner et al., 2017). The most recent studies made since the landing revealed the structure of the top crust on Mars at the InSight landing area to be composed of a variable thickness (cm) duricrust overlaying ~2–3 m layer regolith that grades with depth into coarse blocky material overlying fractured basalt flows (Banerdt et al., 2020; Golombek et al., 2020). In this study, we include a range of porosity values to mimic the near-surface properties, however, for simplicity we only consider uniform, single layer targets, as possible end members for the upper tens of meters of Mars.

The mechanical target properties were combined from landing site observations and experimental and numerical modeling data (Borg et al., 2005; Güldemeister & Wünnemann, 2017; Morgan et al., 2018; Wójcicka et al., 2020). We simulated bedrock (0% porosity), fractured bedrock (with 25% porosity), and regolith (with 44% and 65% porosity). We used the ROCK strength model (Collins et al., 2004) to describe the shear strength of intact and fractured bedrock. The material model for fractured bedrock was assumed similar to sandstone (Güldemeister & Wünnemann, 2017). The Lundborg strength model (Lundborg, 1968) was used to describe the strength of regolith (Table 1). To keep a consistent and realistic ratio between the crushing strength and cohesion, we varied the cohesion for each porosity case (see also, Wójcicka et al., 2020). The cohesion is the shear strength at zero pressure. The crushing strength is the strength at onset of permanent compaction. While the two are likely related and comparable in magnitude, they are not the same or directly linked through the material model. The crushing strength, Yc is approximately defined as $Yc = \varepsilon B\chi / \alpha$, where ε is the elastic threshold volume strain, B is the bulk modulus of the nonporous target material, χ is the ratio of the speed of sound in porous and nonporous medium, and α is the distension in the target. Distension represent porosity in ε–α porosity model as $\alpha = 1 / \left(1 - \varphi\right)$, where φ is porosity. We varied cohesion and crushing strength so that the ratio between them stays close to a physically sensible value. Here, we used about 10, but readjusting so that other porosity parameters are kept as realistic as possible. Some level of estimation was necessary given the lack of relevant experimental data/analog materials.

Rock model for damaged material in iSALE-2D is described as (Collins et al., 2004) $Y = Y_d D + Y_i\left(1 - D\right)$, where Y is the yield strength, Y_d is the shear strength, Y_i is the intact strength (cohesion), and D is a scalar measure of damage (where $D = 0$ means intact and $D = 1$ means damaged). The Lundborg strength model for damaged material (LUNDD, Table 1) defines the yield strength Y as (Collins et al., 2004)

$$Y = Y_0 + \frac{\mu p}{1 + \frac{\mu p}{Y_m - Y_0}}$$

where μ is the coefficient of internal friction, p is the applied pressure, Y_m is the limiting strength, and Y_0 is the cohesion (yield strength at zero pressure).

We used the ε–α porosity model (Collins et al., 2011; Wünnemann et al., 2006) to describe the compaction and compression of pore space (Table 2), and we used the material models used in previous work for highly porous silica sand (Miljković et al., 2011; Wójcicka et al., 2020).

The ε–α porous compaction model (Collins et al., 2011; Wünnemann et al., 2006) shows distension (α) as a function of volumetric strain (ε). A shock wave traveling through the target crushes pore space and compacts and compresses the target. The basic concept of ε–α compaction model describes compression of porous material to fully consolidated state through four regimes: (a) elastic compaction: $\alpha = \alpha_0$, where α_0 is initial distension; (b) exponential compaction: $\alpha = \alpha_0 e^{k\left(\varepsilon - \varepsilon_e\right)}$, where ε_e is volume strain at the elastic limit (onset of plastic compaction); (c) power law compaction: $\alpha = 1 + \left(\alpha_x - 1\right)\left(\frac{\varepsilon_c - \varepsilon}{\varepsilon_c - \varepsilon_e}\right)^2$, where α_x is distension at transition from exponential to power law compaction; ε_c is volumetric strain at which all pore space is compacted (onset of pure compression); and (d) compression $\alpha = 1$; meaning all pore space is compacted.

Table 2 also includes parameter χ that represents ratio of speed of sound in porous and nonporous medium.

We used the computationally efficient, analytical Tillotson equation of state, EoS, (Tillotson, 1962) with parameters for basalt (Benz & Asphaug, 1999) to represent the nonporous component of the target materials

Table 2
The ε–α Porosity Model Parameters Used in Simulations (Collins et al., 2011; Wunnemann et al., 2006)

Parameter	Target		
	Fractured bedrock (25% porosity)	Highly porous regolith (44% porosity)	Highly porous regolith (65% porosity)
Initial distension, $\alpha = 1 - 1/\rho$	1.33	1.8	2.8
Elastic threshold, marks the start of compaction, ε_0	-4×10^{-4}	-10^{-4}	-10^{-5}
Distension at transition from exponential to power law compaction, α_x	1.1	1.15	1.0
The rate of change of distension with respect to volumetric strain, κ	0.98	0.98	0.98
Ratio of the speed of sound in porous over nonporous medium, χ	0.6	0.33	0.21

and the impactor, considering that our simulations produced relatively low peak shock pressures below the regime of solid-solid phase transformations (Wójcicka et al., 2020) (Table 3).

We used a simplified approach for calculating seismic efficiency that was used in previous studies (Güldemeister & Wünnemann, 2017; Schultz & Gault, 1975): $k = \frac{\pi x^2 P^2 \Delta t}{3\rho CpEk}$, where x represents distance from the impact point, P pressure amplitudes, Δt is duration of the pressure pulse, ρ is the density of the target, Cp is the speed of sound in the target, and Ek is the kinetic energy of the impactor. Using this approach, all parameters can be calculated numerically from the iSALE simulations. The speed of sound was calculated from the bulk modulus of basalt used in the EoS. The speed of sound can be represented as a $c = \sqrt{(B/\rho)}$, where B is bulk modulus ($B = 19.3$ GPa for basalt, from Wójcicka et al. [2020]) and ρ is the rock bulk density (for Martian basalts $\rho = 2860$ kg/m^3). For porous materials, this value is multiplied by the ratio of speed of sound in nonporous rock and porous rock (for 25% it was 0.6, for 44% porosity it was 0.33, and for 65% porosity it was 0.21; Borg et al., 2005; Güldemeister & Wünnemann, 2017; Miljković et al., 2011; Wójcicka et al., 2020). Pressure pulses were isolated from the gauges where their amplitudes (P) and positions were recorded (from position distance from impact point is easily calculated). The duration of the pressure pulse was calculated as a full width at half the maximum. Similar approach was used recently in our study by Wójcicka et al. (2020).

We tested quantifying seismic energy from particle velocities directly from the simulations. Particle velocity is stored in the cells and is easy to calculate. To quantify seismic energy in a cell within the wave, we used equation $Es = \rho v^2 V / 2$, where Es is seismic energy, ρ is density of the target in the cell, υ is particle velocity in the cell, and V is volume of the cell. Then, cells within the wave region were selected according to a pressure amplitude threshold. The seismic efficiency was obtained as $k = Es / Ek$, where Ek is kinetic energy of the impactor.

This approach requires velocity information in the grid to be stored at high precision for the entire calculation, which is impractical for a large number of simulations. Also, this approach introduces some subjectivity since it requires a criterion for identifying the wave region, which is why we preferred the first method even though the two approaches agreed in a test case scenario.

Table 3
Tillotson EoS Parameter for Basalt (Benz & Asphaug, 1999; Wójcicka et al., 2020)

Parameter	Value
Reference density (kg/m^3)	2,860
Spec. heat capacity (K/kg/K)	1,000
Bulk modulus (Pa)	1.93×10^{10}
Tillotson B constant (Pa)	2.93×10^{10}
Tillotson $E0$ constant (J/kg)	4.87×10^{8}
Tillotson a constant	0.5
Tillotson b constant	0.8
Tillotson alpha constant	5.0
Tillotson beta constant	5.0
Specific internal energy, incipient vaporization (J/kg)	4.72×10^{6}
Specific internal energy, complete vaporization (J/kg)	18.2×10^{6}

3. Results

For modeling of the pressure wave propagation to its elastic regime, the pressure wave needs to be tracked to distances larger than usually used in a crater formation simulation. Thus, a simulation requires a large computational mesh. However, previous studies recommended using a high CPPR value for accurate estimates of peak pressure in nonporous

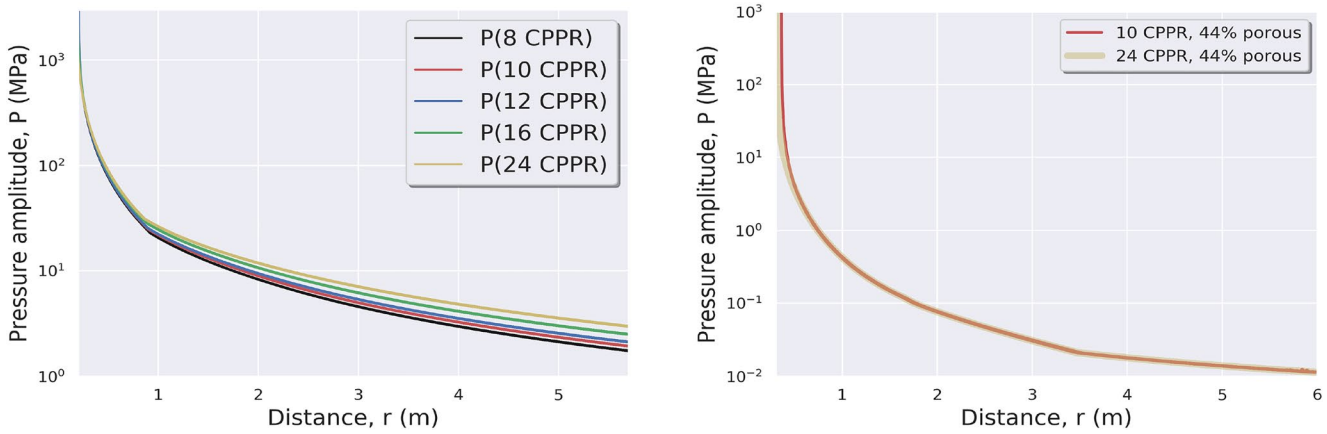

Figure 1. Pressure decay with distance, measured diagonally through the target starting from the impact point. (left) For the nonporous target, the ratio between 10 CPPR and 24 CPPR at the several crater radii distance is ~0.6. (right). For the 44% porous target, no resolution effects were observed between 10 and 24 CPPR. CPPR, computational cells per projectile radius.

quartzite targets (Güldemeister & Wünnemann, 2017; Wünnemann et al., 2008), which is not practical when a large mesh is necessary. Pierazzo et al. (2008) recommended resolution of 20 CPPR or higher in aluminum targets and Güldemeister and Wünnemann (2017) recommended value of 24 CPPR as sufficient for accurate estimates of pressure amplitude decay in quartzite targets. Considering our computational domain is more than 10 times larger than applied in Güldemeister and Wünnemann (2017), we used 10 CPPR as the lowest sensible resolution. However, we quantified difference in pressure amplitudes between the 10 CPPR (low resolution) and 24 CPPR (high resolution) for both nonporous rock and 44% regolith simulant (Figure 1). The resolution tests were made for the 1.5 m crater, simulated using a spherical projectile 4.4 cm in diameter hitting a target made of basalt with 0% and 44% porosity at 2 km/s. Simulation results showed that the pressure amplitudes in a nonporous target were lower by about 40% when low resolution was applied compared to the higher resolution assumed to produce a more accurate pressure estimate. Such a pressure amplitude drop agrees with previous works (Güldemeister & Wünnemann, 2017; Pierazzo et al., 2008). However, when 44% is applied in the target, the pressure difference between the low-resolution and high-resolution runs remained unchanged. The consumption of impact energy and the reduction of pressure amplitude is more effectively made by the presence of pore space, which resulted in resolution effect only being visible in the nonporous case. Furthermore, the resolution was shown not to have an effect on other properties of the pressure propagation, such are the duration and speed of the pressure pulse.

Figure 2 shows the pressure wave propagation for the 0% (a), 25% (b), 44% (c), and 65% (d) target porosities, during the excavation stage of the 1.5-m diameter crater. The kinetic energy of the impactor was kept constant, $Ek = 1.8 \times 10^6$ J made by 4.4 cm impactor at 2 km/s, in all four cases. The pressure wave was captured at a similar distance from the impact point, to demonstrate greater pressure amplitude decrease with the increase in porosity.

Figure 3 (left) shows that the larger the porosity, the larger the decrease in the pressure amplitudes at the several crater radii distance. More specifically, we found that the pressure amplitudes in the 25% case to be about an order magnitude higher than in the 65% porosity target, in the elastic regime, while pressure amplitudes in the 44% case are about 3 times higher than in the case of the 65% porosity. Figure 3 (right) shows the pressure amplitudes normalized to 0% porosity case significantly decreasing with the increase of porosity at the several crater radii distance.

The seismic efficiency, k, was calculated for the reference 1.5 m crater recently observed on Mars, for all target models considered in this work. Seismic efficiency was calculated at a distance of several crater radii. At this distance, pressure amplitudes were at least half an order magnitude lower than the crushing strength, which we consider here to be the transition from the plastic or shock regime to the elastic regime. In addition, Holsapple (1993) defines the strong shock regime when particle velocity in the target is much larger than the speed of sound in the target ($P >> \rho c^2$, where P is the pressure amplitude, ρ is density of the

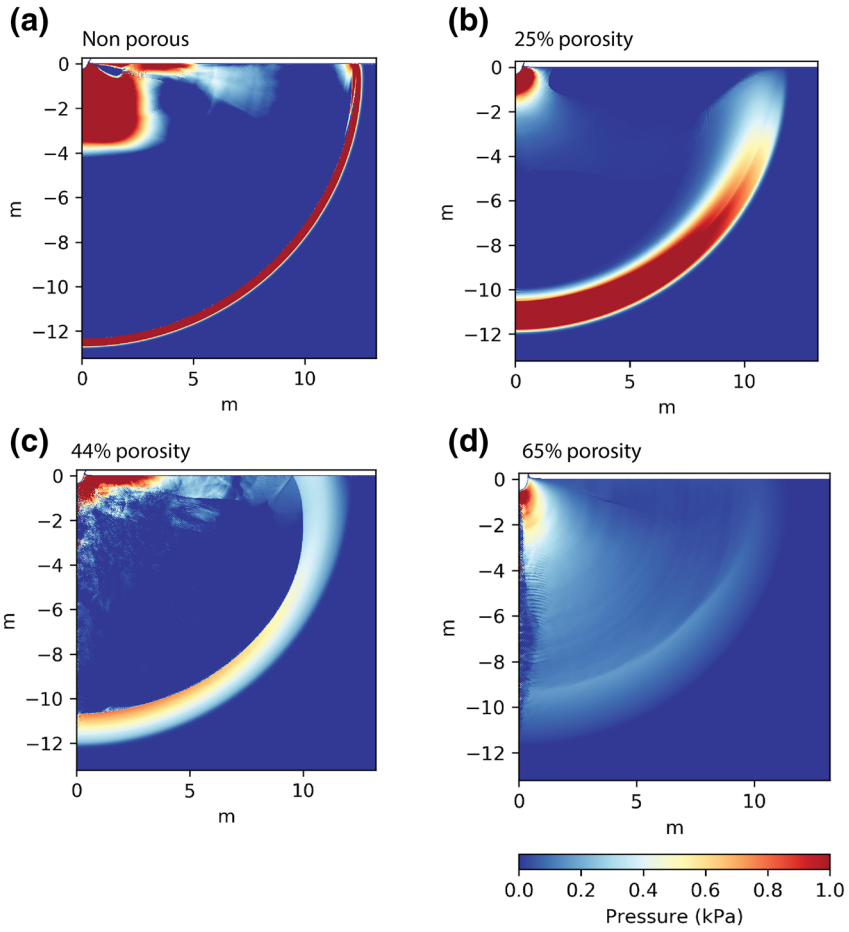

Figure 2. Impact simulations results show the pressure wave decay through the target with: (a) 0%, (b) 25%, (c) 44%, and (d) 65% porosity, captured ~12 m away from the impact point.

target, and c is the speed of sound in the target) and suggests that the pressure amplitude decays quickly as a function of distance with the power exponent of −3.6 in this regime. As the pressure propagation further decays with distance, the pressure amplitude becomes comparable to ρc^2. This represents the intermediate

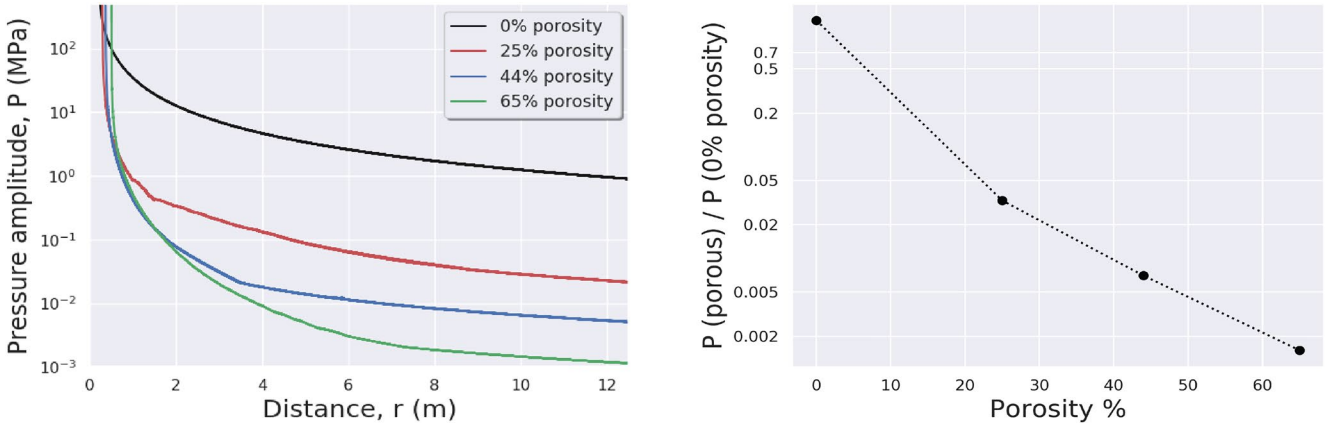

Figure 3. (Left) The pressure amplitude decay with distance in 0% (black line), 25% (red line), 44% (blue line), and 65% (green line) porosity target. This is for same impact conditions shown in this figure. (Right) The pressure amplitudes normalized to 0% porosity case at 10 m distance from impact point to demonstrate the decrease in pressures with the increase of porosity.

Table 4
Seismic Efficiency Values From Our Simulations, and Compared to Previous Studies (NM Refers to Numerical Modeling, EXP to Impact Experiments, and UE for Underground Explosions)

Author	Method	Material (porosity)	Seismic efficiency, k	Duration of the pressure pulse, $\Delta t\,(s)$	Pressure amplitude, $P\,(Pa)$	Distance from the impact point, $x\,(m)$
This work	NM	Basalt (0%)	7.8×10^{-4}	5.36×10^{-5}	802897.20	13.08
	NM	Basalt (25%)	3.9×10^{-6}	3.44×10^{-4}	19579.68	13.08
	NM	Basalt (44%)	1.52×10^{-6}	9.50×10^{-4}	5787.65	13.08
	NM	Basalt (65%)	4.4×10^{-7}	2.23×10^{-3}	1052.63	13.08
Güldemeister and Wünnemann, 2017	NM	Quarzite (0%)	3.39×10^{-3}			
	NM	SS (25%)	2.56×10^{-3}			
	NM	Tuff (43%)	2.02×10^{-3}			
	NM	Sandstone (12%)	3.00×10^{-3}			
	NM	Sandstone (35%)	2.18×10^{-3}			
	NM	Sandstone (50%)	2.20×10^{-3}			
Wójcicka et al., 2020	NM	Basalt (44%)	$\sim 10^{-6}$			
Yasui et al., 2015	EXP	Glass beads (40%)	$10^{-5} - 10^{-4}$			
Hoerth et al., 2014	EXP	Sandstone (25%)	$\sim 5 \times 10^{-3}$			
McGarr et al., 1969	EXP	Bonded sand (sand grains bonded by epoxy cement)	$10^{-5} - 10^{-4}$			
Latham et al., 1970	Apollo 12/13 drops	Lunar regolith (50+/−15%)	$10^{-6} - 10^{-5}$			
Patton and Walter, 1993	UE	Different media (tuff, granite, shale, salt)	$10^{-2} - 10^{-1}$			

regime, where Holsapple (1993) calculated the pressure decay with the distance to be at the power of −1.8. In far field, the pressure continues to decay comparably either to the material strength or to initial pressure. This is the material strength regime and Holsapple (1993) suggested that the pressure decays with distance to the power of −1.18. Pressure amplitude decay presented at Figure 3 compared to the material strength from Table 1 implies that pressure wave is out of shock and intermediate regime. Simulations showed that there is a clear decrease in seismic efficiency with increasing porosity: k is $\approx 10^{-4}$ for the nonporous bedrock and $\approx 10^{-6}$ for the fractured bedrock and highly porous regolith (Table 4). Results presented in Table 4 include the correction factor of 1.7 in the nonporous case to account for the resolution effects that produced lower pressure amplitudes (Figure 1). Table 4 also includes a comparison with previous works that have also suggested that the seismic efficiency in the impact cratering process should be dependent on the target properties.

Previous works suggested that the seismic efficiency could also depend on the crushing strength (i.e., the pressure required to cause permanent compaction) in the target medium (Güldemeister & Wünnemann, 2017). Therefore, this work methodically investigated the sensitivity of seismic efficiency to the parameters used in the ε–α porosity model that control the crushing strength and the speed of sound in the pristine porous material. In the reference case for the 44% target porosity with parameters given in Tables 1 and 2, the seismic efficiency was 1.5×10^{-6}. The speed of sound ratio was 0.33 and the elastic strain threshold −0.0001 (Table 2). Table 5 shows the combination of varied parameters: (a) the speed of sound was fixed when the elastic threshold and cohesion were varied by an order magnitude, and (b) the elastic threshold was kept fixed but the cohesion and the speed of sound was changed.

As expected, increasing the speed of sound ratio reduced the arrival time and the duration of the pressure pulse (Figure 4), both of which reduce the seismic efficiency. If the speed of sound ratio were as high as 0.5 (meaning that the speed of sound in the porous target was 50% of the speed of sound in a nonporous case), the value of seismic efficiency was estimated lower 3.26×10^{-8} then the one estimated in the reference case.

Table 5
Varied Parameters in Porosity Model and Resulting Seismic Efficiency

	Cohesion, Y_0 (kPa)	Crushing strength (kPa)	Elastic threshold, ε_0	Speed of sound ratio, χ	Seismic efficiency, k
Ref. case	10	117	10^{-4}	0.33	1.52×10^{-6}
a	100	1.17×10^{3}	10^{-3}	0.33	4.6×10^{-6}
	1	17	10^{-5}	0.33	8.15×10^{-7}
b	4	40	10^{-4}	0.2	1.9×10^{-6}
	27	270	10^{-4}	0.5	3.26×10^{-8}

If the speed of sound ratio were as low as 0.2 (Figure 4a), the seismic efficiency was estimated 1.9×10^{-6} (Table 5). Both values are in the same order of magnitude.

Increasing the crushing pressure, on the other hand, increased the pressure pulse amplitude but decreased the duration of the pressure pulse (Figure 5), which have competing influences on seismic efficiency. For the scenarios investigated here, the former effect dominates, so that seismic efficiency is substantially higher in materials with a higher crushing strength. For elastic threshold set at −0.001 in 44% porous case, the value of seismic efficiency was 4.6×10^{-6} (Table 5). This is over half an order of magnitude higher than in our porous cases where we used value that is an order of magnitude lower (−0.0001) for the same impact energy. For an order magnitude lower value for the elastic threshold (−0.00001), the seismic efficiency decreased for more than an order of magnitude up to 8.15×10^{-7}, which suggests that the lower the elastic threshold, the lower the seismic efficiency (Table 5).

4. Discussion

Figure 6 shows the summarized results for the seismic efficiency compared to previously published data. Seismic efficiencies calculated in our porous target scenarios are in the same order of magnitude as data obtained from the Moon (Latham et al., 1970) and experimental data acquired by McGarr et al. (1969). Deviations from in Güldemeister and Wünnemann (2017) work are probably due to the fact that in their models they used cohesive targets with much higher strengths and therefore, higher elastic thresholds. Our results are consistent with values determined by Wójcicka et al. (2020) for porous 44% basalt regolith, using the same material model. The difference between porous and nonporous targets in our work is more than 2 orders of magnitude for the seismic efficiency.

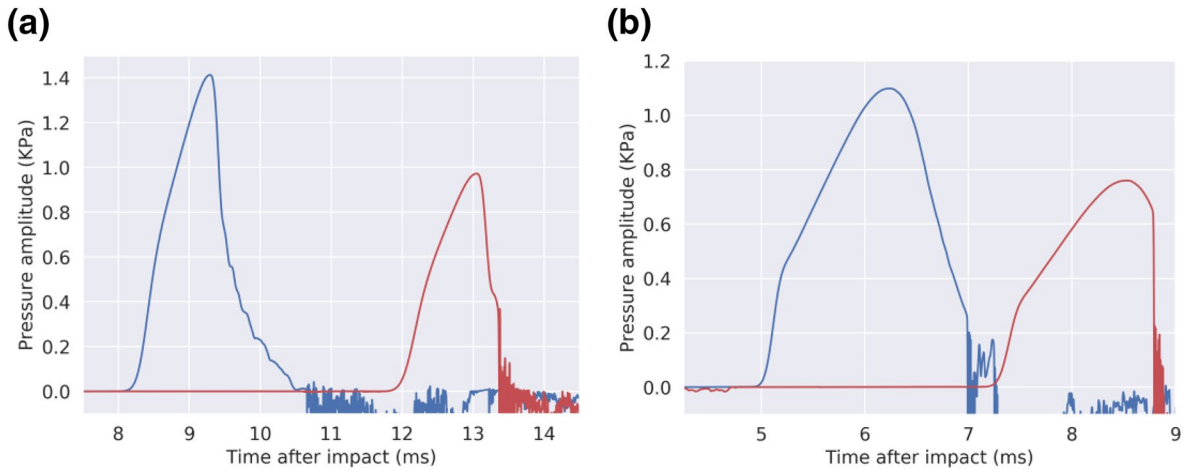

Figure 4. Isolated pressure pulses from different examples of speed of sound ratio applied in the ε–α porosity model. Different colors are isolated pressure pulses from two neighboring gauges. The speed of sound ratio was (a) 0.2 and (b) 0.3 (values used in this work).

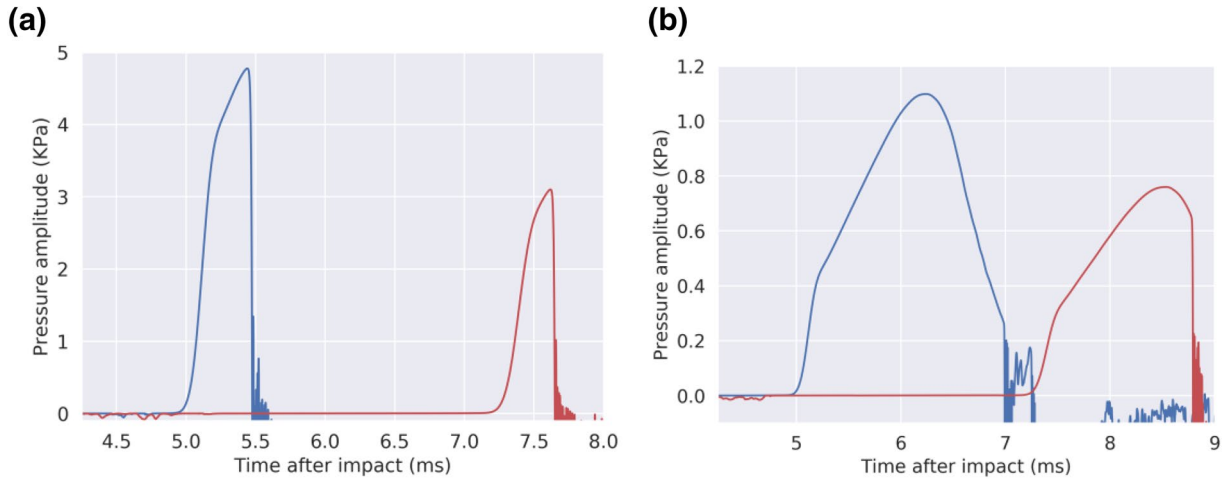

Figure 5. Isolated pressure pulses with different dependence on the elastic threshold applied in the ε–α porosity model as the strain threshold for the start of compaction. Different colors are isolated pressure pulses from two neighboring gauges. The pressure wave profile in the 44% porous basaltic target was made with impact energy 1.8×10^6 J and varied elastic threshold: (a) −0.001 and (b) −0.0001 (value used in this work).

This 1.5 m crater was estimated not to have excavated more than the top 0.5 m of the crust. At the InSight landing area, the top meter is described as porous regolith. This regolith overlays coarse blocky ejecta that grades with depth into fractured basalt (Golombek et al., 2020). From the latest InSight observations, it was inferred that the speed of sound in the top meter of the crust is ~120 m/s; however, the speed of sound increases to 750–1,000 m/s at 5–10 m depth (Lognonné et al., 2020). If the target media is similar at the InSight landing area and the local area where the 1.5 m crater formed, then the crater should have formed in the very porous near-surface regolith, but the pressure propagation zone would extend to a few m depth. The impact energy is mostly absorbed within the crater formation region (Figure 3), therefore, we expect that the high porosity cases presented in this work should be an appropriate representation of the target for the observed 1.5 m crater. Should the crater have been larger, the layering could have had a more dominant effect. This also implies that the detectability of craters formed in the very top crust could be even harder to detect that what was expected before (I. Daubar et al., 2018; Teanby, 2015). This agrees with I. J. Daubar et al. (2020) and Wójcicka et al. (2020) and why it was probably no possible to detect these small impacts on Mars. For crater this size on Mars, the seismic efficiency would be at the order of 10^{-6}.

Furthermore, this work confirmed the decrease of the seismic efficiency with increase of porosity and places end member seismic efficiency values for a large range of target porosities. For the investigated range of target properties assumed for a Martian surface analog, we estimated seismic efficiency to be between 10^{-7} and 10^{-3}. Given that the seismic efficiency could vary up to 4 orders of magnitude or more is a strong indicator that the seismic detectability of impacts will depend on the area where impact occurs.

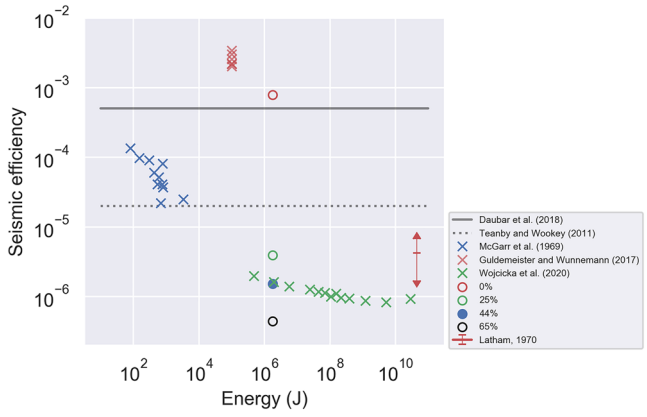

Figure 6. Different impact scenarios and how seismic efficiency varies with impact energy.

5. Conclusions

In this study, we investigated seismic efficiency for small impact cratering process into different Martian upper crust simulants. In previous works, I. Daubar et al. (2018) approximated the seismic efficiency to be 5×10^{-4} for the Martian environment. We calculated that the seismic efficiency in meter-size impacts on Mars is different between bedrock (~10^{-4}) and porous materials (~10^{-6}). The seismic efficiency decreases with the increase of porosity in the target medium. Therefore, our results suggested that impacts on hard, rock-like surfaces on Mars will be significantly more detectable than impacts in regolith. Such a result contributes to the

understanding of the new low number of detectable impact craters on Mars during the lifetime of the InSight mission (I. J. Daubar et al., 2020).

Furthermore, we investigated the sensitivity of the seismic efficiency on the numerical setting, such as the parameters used in the porosity models and the computational mesh resolution. We showed that the seismic efficiency depends on crushing strength, elastic threshold, and speed of sound in the target. These parameters affect pressure wave amplitudes and duration of the pressure pulse which are both used in calculation of seismic efficiency. Higher crushing strength and elastic threshold result in higher seismic efficiencies. Same, with increasing speed of sound ratio in the target, seismic efficiency decreases. In impact experiments in to sand, studies (e.g., Matsue et al., 2020) showed that seismic energy still drops at 10 crater radii. In our numerical study, we quantify seismic efficiency at the 22 crater radii distance. At this distance, it is suggested that we have conservation of the seismic energy. Seismic dissipation at different frequencies could also have an effect, however, that was not investigated here. Nevertheless, our data represent an upper bound for seismic efficiency in different Martian upper crust simulants.

The standard computational mesh resolution used for simulating crater formation is shown to reduce pressure wave amplitudes by 60% in case of nonporous targets. However, it was found that the resolution does not change pressure amplitudes in case of porous target. This work has shown the importance of using validated material models and has emphasized which parameters affect the pressure propagation, and therefore, the seismic efficiency the most.

Data Availability Statement

All the data used in this study can be found at Rajšić, A. (2020). Seismic efficiency of meteoroid strikes in Martian bedrock and regolith (https://doi.org/10.5281/ZENODO.3992873).

Acknowledgments
A. Rajšić is fully supported by the Australian Research Council on DE180100584. K. Miljković is fully supported by the Australian Research Council on DP180100661 and DE180100584. K. Wünnemann and M. A. Wieczorek are supported by DP180100661 via Discovery International Award. We gratefully acknowledge the iSALE code developers (https://isale-code.github.io/). This manuscript has InSight contribution number 169.

References

Amsden, A. A., Ruppel, H. M., & Hirt, C. W. (1980). *SALE: A simplified ALE computer program for fluid flow at all speeds (Rep. LA-8095)*. Los Alamos, NM: Los Alamos National Laboratory.

Banerdt, W. B., Smrekar, S. E., Banfield, D., Giardini, D., Golombek, M., Johnson, C. L., et al. (2020). Initial results from the InSight mission on Mars. *Nature Geoscience*, *13*, 183–189.

Benz, W., & Asphaug, E. (1999). *Catastrophic disruptions revisited*. arXiv preprint astro-ph/9907117.

Borg, J. P., Chapman, D. J., Tsembelis, K., Proud, W. G., & Cogar, J. R. (2005). Dynamic compaction of porous silica powder. *Journal of Applied Physics*, *98*(7), 073509.

Collins, G. S., Melosh, H. J., & Ivanov, B. A. (2004). Modeling damage and deformation in impact simulations. *Meteoritics & Planetary Science*, *39*(2), 217–231.

Collins, G. S., Melosh, H. J., & Marcus, R. A. (2005). Earth impact effects program: A web-based computer program for calculating the regional environmental consequences of a meteoroid impact on Earth. *Meteoritics & Planetary Science*, *40*(6), 817–840.

Collins, G. S., Melosh, H. J., & Wünnemann, K., (2011). Improvements to the ε–α porous compaction model for simulating impacts into high-porosity solar system objects. *International Journal of Impact Engineering*, *38*, 434–439. https://doi.org/10.1016/j.ijimpeng.2010.10.013

Cox, M. A., Cavosie, A. J., Ferrière, L., Timms, N. E., Bland, P. A., Miljković, K., et al. (2019). Shocked quartz in polymict impact breccia from the Upper Cretaceous Yallalie impact structure in Western Australia. *Meteoritics & Planetary Science*, *54*(3), 621–637.

Daubar, I., Lognonné, P., Teanby, N. A., Miljković, K., Stevanović, J., Vaubaillon, J., et al. (2018). Impact-seismic investigations of the InSight mission. *Space Science Reviews*, *214*(8), 132. https://doi.org/10.1007/s11214-018-0562-x

Daubar, I. J., Atwood-Stone, C., Byrne, S., McEwen, A. S., & Russell, P. S. (2014). The morphology of small fresh craters on Mars and the Moon: Fresh Crater d/D on Mars and the Moon. *Journal of Geophysical Research: Planets*, *119*, 2620–2639. https://doi.org/10.1002/2014JE004671

Daubar, I. J., Lognonné, P., Teanby, N. A., Malin, M., Posiolova, L., McEwen, A. S., et al. (2020). A new crater near InSight: Implications for seismic impact detectability on Mars. *Journal of Geophysical Research: Planets*, *125*, e2020JE006382. https://doi.org/10.1029/2020JE006382

Daubar, I. J., McEwen, A. S., Byrne, S., Kennedy, M. R., & Ivanov, B. (2013). The current Martian cratering rate. *Icarus*, *225*(1), 506–516. https://doi.org/10.1016/j.icarus.2013.04.009

Golombek, M., Kipp, D., Warner, N., Daubar, I. J., Fergason, R., Kirk, R. L., et al. (2017). Selection of the InSight landing site. *Space Science Reviews*, *211*(1–4), 5–95.

Golombek, M., Warner, N. H., Grant, J. A., Hauber, E., Ansan, V., Weitz, C. M., et al. (2020). Geology of the InSight landing site on Mars. *Nature Communications*, *11*(1), 1–11.

Güldemeister, N., & Wünnemann, K. (2017). Quantitative analysis of impact-induced seismic signals by numerical modeling. *Icarus*, *296*, 15–27. https://doi.org/10.1016/j.icarus.2017.05.010

Hoerth, T., Schäfer, F., Nau, S., Kuder, J., Poelchau, M. H., Thoma, K., & Kenkmann, T. (2014). In situ measurements of impact-induced pressure waves in sandstone targets: Impact-induced pressure waves. *Journal of Geophysical Research: Planets*, *119*, 2177–2187. https://doi.org/10.1002/2014JE004616

Holsapple, K. A. (1993). The scaling of impact processes in planetary sciences. *Annual Review of Earth and Planetary Sciences*, *21*(1), 333–373.
Holsapple, K. A., & Housen, K. R. (2007). A crater and its ejecta: An interpretation of deep impact. *Icarus*, *191*(2), 586–597.
Knapmeyer-Endrun, B., Golombek, M. P., & Ohrnberger, M. (2017). Rayleigh wave ellipticity modeling and inversion for shallow structure at the proposed InSight landing site in Elysium Planitia, Mars. *Space Science Reviews*, *211*(1–4), 339–382. https://doi.org/10.1007/s11214-016-0300-1
Latham, G., Ewing, M., Dorman, J., Press, F., Toksoz, N., Sutton, G., et al. (1970). Seismic data from man-made impacts on the Moon. *Science*, *170*(3958), 620–626.
Lognonné, P., Banerdt, W. B., Pike, W. T., Giardini, D., Christensen, U., Garcia, R. F., et al. (2020). Constraints on the shallow elastic and anelastic structure of Mars from InSight seismic data. *Nature Geoscience*, *13*(3), 213–220.
Lundborg, N. (1968). Strength of rock-like materials. *International Journal of Rock Mechanics and Mining Sciences*, *5*, 427–454.
Malin, M. C., Edgett, K. S., Posiolova, L. V., McColley, S. M., & Dobrea, E. Z. N. (2006). Present-day impact cratering rate and contemporary gully activity on Mars. *Science*, *314*(5805), 1573–1577.
Matsue, K., Yasui, M., Arakawa, M., & Hasegawa, S. (2020). Measurements of seismic waves induced by high-velocity impacts: Implications for seismic shaking surrounding impact craters on asteroids. *Icarus*, *338*, 113520. https://doi.org/10.1016/j.icarus.2019.113520
McGarr, A., Latham, G. V., & Gault, D. E. (1969). Meteoroid impacts as sources of seismicity on the Moon. *Journal of Geophysical Research*, *74*(25), 5981–5994. https://doi.org/10.1029/JB074i025p05981
McMullan, S., & Collins, G. S. (2019). Uncertainty quantification in continuous fragmentation airburst models. *Icarus*, *327*, 19–35. https://doi.org/10.1016/j.icarus.2019.02.013
Miljković, K., Collins, G., Patel, M., Chapman, D., & Proud, W. (2011). *High-velocity impacts in regolith: Insight from numerical models and experiments* (CKH-40). American Physical Society.
Miljković, K., Teanby, N. A., Daubar, I. J., Lognonné, P., & Wieczorek, M. A. (2019). Numerical investigation of impact-induced seismic signals in Martian crust. In *Lunar and Planetary Science Conference 50*, abstract 1503.
Morgan, P., Grott, M., Knapmeyer-Endrun, B., Golombek, M., Delage, P., Lognonné, P., et al. (2018). A pre-landing assessment of regolith properties at the InSight landing site. *Space Science Reviews*, *214*(6), 104. https://doi.org/10.1007/s11214-018-0537-y
Patton, H. J., & Walter, W. R. (1993). Regional moment:magnitude relations for earthquakes and explosions. *Geophysical Research Letters*, *20*(4), 277–280. https://doi.org/10.1029/93GL00298
Pierazzo, E., Artemieva, N., Asphaug, E., Baldwin, E. C., Cazamias, J., Coker, R., et al. (2008). Validation of numerical codes for impact and explosion cratering: Impacts on strengthless and metal targets. *Meteoritics & Planetary Science*, *43*(12), 1917–1938.
Pierazzo, E., Vickery, A. M., & Melosh, H. J. (1997). A reevaluation of impact melt production. *Icarus*, *127*(2), 408–423.
Pomeroy, P. W. (1963). Long period seismic waves from large, near-surface nuclear explosions. *Bulletin of the Seismological Society of America*, *53*, 109–149.
Prieur, N. C., Rolf, T., Luther, R., Wünnemann, K., Xiao, Z., & Werner, S. C. (2017). The effect of target properties on transient crater scaling for simple craters. *Journal of Geophysical Research: Planets*, *122*, 1704–1726. https://doi.org/10.1002/2017JE005283
Richardson, J. E., & Kedar, S. (2013). An experimental investigation of the seismic signal produced by hypervelocity impacts. In Lunar and Planetary Science Conference 44, abstract 2863.
Schmidt, R. M., & Housen, K. R. (1987). Some recent advances in the scaling of impact and explosion cratering. *International Journal of Impact Engineering*, *5*(1–4), 543–560.
Schultz, P. H., & Gault, D. E. (1975). Seismic effects from major basin formations on the moon and mercury. *The Moon*, *12*(2), 159–177. https://doi.org/10.1007/BF00577875
Shishkin, N. I. (2007). Seismic efficiency of a contact explosion and a high-velocity impact. *Journal of Applied Mechanics and Technical Physics*, *48*(2), 145–152. https://doi.org/10.1007/s10808-007-0019-6
Stevanović, J., Teanby, N. A., Wookey, J., Selby, N., Daubar, I. J., Vaubaillon, J., & Garcia, R. (2017). Bolide airbursts as a seismic source for the 2018 Mars InSight mission. *Space Science Reviews*, *211*(1), 525–545. https://doi.org/10.1007/s11214-016-0327-3
Tanaka, K. L., Robbins, S. J., Fortezzo, C. M., Skinner, J. A., Jr., & Hare, T. M. (2014). The digital global geologic map of Mars: Chronostratigraphic ages, topographic and crater morphologic characteristics, and updated resurfacing history. *Planetary and Space Science*(95), 11–24.
Teanby, N. A. (2015). Predicted detection rates of regional-scale meteorite impacts on Mars with the InSight short- period seismometer. *Icarus*, *256*, 49–62.
Teanby, N. A., & Wookey, J. (2011). Seismic detection of meteorite impacts on Mars. *Physics of the Earth and Planetary Interiors*, *186*(1–2), 70–80. https://doi.org/10.1016/j.pepi.2011.03.004
Tillotson, J. H. (1962). *Metallic equations of state for hypervelocity impact*. San Diego, CA: General Dynamics.
Warner, N. H., Golombek, M. P., Sweeney, J., Fergason, R., Kirk, R., & Schwartz, C. (2017). Near surface stratigraphy and regolith production in southwestern Elysium Planitia, Mars: Implications for Hesperian–Amazonian Terrains and the InSight lander mission. *Space Science Reviews*, *211*(1), 147–190. https://doi.org/10.1007/s11214-017-0352-x
Wójcicka, N., Collins, G. S., Bastow, I., Miljkovic, K., Teanby, N. A., Karakostas, F., & Lognonné, P. (2020). The seismic moment and seismic efficiency of small impacts on Mars. *Journal of Geophysical Research: Planets*, *125*, e2020JE006540. https://doi.org/10.1029/2020JE006540
Wünnemann, K., Collins, G. S., & Melosh, H. J. (2006). A strain-based porosity model for use in hydrocode simulations of impacts and implications for transient crater growth in porous targets. *Icarus*, *180*(2), 514–527. https://doi.org/10.1016/j.icarus.2005.10.013
Wünnemann, K., Collins, G. S., & Osinski, G. R. (2008). Numerical modeling of impact melt production in porous rocks. *Earth and Planetary Science Letters*, *269*(3–4), 530–539. https://doi.org/10.1016/j.epsl.2008.03.007
Wünnemann, K., Nowka, D., Collins, G. S., Elbeshausen, D., & Bierhaus, M. (2011). Scaling of impact crater formation on planetary surfaces—Insights from numerical modeling. In *Proceedings of the 11th hypervelocity impact symposium* (Vol. 120, pp. 1–16). Fraunhofer Verlag.
Yasui, M., Matsumoto, E., & Arakawa, M. (2015). Experimental study on impact-induced seismic wave propagation through granular materials. *Icarus*, *260*, 320–331. https://doi.org/10.1016/j.icarus.2015.07.032
Zel'dovich, Y. B., & Raizer, Y. P. (2012). *Physics of shock waves and high-temperature hydrodynamic phenomena*. Courier Corporation.